

AD-A101 519      NAVAL RESEARCH LAB WASHINGTON DC  
NEUTRON-INDUCED REACTIONS IN TISSUE-RESIDENT ELEMENTS, (U)  
JUL 81   G H HERLING, R H BASSEL, J H ADAMS  
UNCLASSIFIED   NRL-8441

F/6 6/18

NL

1 of 1  
AN 4  
1-21518

END  
8-81  
DTIC

ADA101519

*12*  
NRL Report 8441 ✓

## Neutron-Induced Reactions in Tissue-Resident Elements

G. H. HERLING, R. H. BASSEL, J. H. ADAMS,  
AND W. A. FRASER

*Radiation-Matter Interactions Branch  
Condensed Matter and Radiation Sciences Division*

DTIC  
SELECT  
JUL 17 1981  
C



NAVAL RESEARCH LABORATORY  
Washington, D.C.

Approved for public release; distribution unlimited.

81 7 17 005

35  
DTIC FILE COPY

NRL - 7-1

12

SECURITY CLASSIFICATION OF THIS PAGE (When Data Entered)

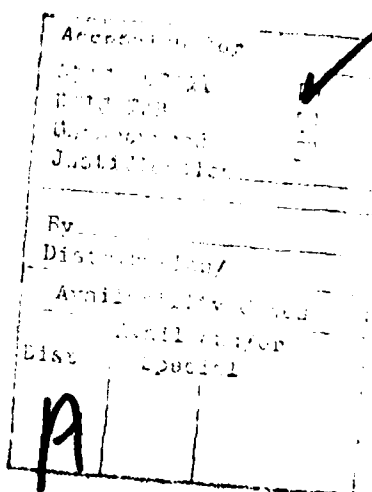
DD FORM 1 JAN 73 1473

EDITION OF 1 NOV 65 IS OBSOLETE  
S/N 0102-014-6601

SECURITY CLASSIFICATION OF THIS PAGE (When Data Entered)

## CONTENTS

1. INTRODUCTION .....	1
2. ENERGY TRANSFER TO HYDROGEN .....	2
3. THEORETICAL MODELS FOR COMPLEX NUCLEI .....	2
A. Optical Model .....	2
B. Inelastic Scattering .....	3
C. Analogue Inelastic Scattering Model .....	3
D. The $(n,d)$ , $(n,t)$ , $(n, {}^3\text{He})$ Reactions .....	4
E. Compound Nucleus Reactions .....	5
4. RESULTS FOR INDIVIDUAL ELEMENTS .....	6
A. Carbon .....	6
B. Oxygen .....	10
C. Nitrogen .....	15
5. KERMA FACTORS .....	17
6. CONCLUSION .....	18
7. ACKNOWLEDGMENTS .....	19
REFERENCES .....	19



## NEUTRON-INDUCED REACTIONS IN TISSUE-RESIDENT ELEMENTS

### 1. INTRODUCTION

In 1973, encouraging results for the neutron radiotherapy treatment of cancer were reported from the Hammersmith Hospital at the Conference on Particle Accelerators in Radiation Therapy [1]. At the same conference, preliminary studies with the objective of establishing controlled clinical trials in the United States were also reported [2,3]. Such trials have been undertaken at the Naval Research Laboratory in collaboration with George Washington University, at Texas A&M University in collaboration with the M. D. Anderson Hospital, at NASA Lewis Research Center in collaboration with Case Western Reserve University, at Fermilab in collaboration with the University of Chicago, and at a number of centers in other countries.

These studies have shown that the dose with fast neutrons has been found to be apparently more critical than that with conventional megavoltage radiation, with the consequence that there is an increased demand for high-precision, high-accuracy dosimetry in mixed neutron and gamma radiation fields. In order to satisfy this demand, standardization of dosimetry has been studied by having representatives from a number of centers perform measurements in a common, prescribed radiation field [4,5]. The users of homogeneous tissue-equivalent ionization chambers generally obtained results in the INDI project which were within 5% of the mean value for tissue kerma in free air and absorbed dose in a matrix phantom [4] but: "...This variation is probably not acceptable since it is generally necessary for radiotherapy and radiobiology to know absorbed doses to within an overall uncertainty of 5%, which requires the basic dosimetry to be significantly better than this," [5]. It is noted that the standard fields that have been employed are produced by the  $d(t,n)\alpha$  reaction at low energies which results in nearly monoenergetic neutrons with an energy not too far removed from 14 MeV. This energy region has been and is being intensively studied because of nuclear fission, fusion, and weapons effects [6].

The neutron beams at some centers, however, have spectra which lie largely at energies greater than, say, 15 MeV. The previously mentioned dosimetric problem becomes compounded at these higher energies because of the lack of detailed neutron cross-section data. Thus, energy-dependent corrections which might be applied to the basic dosimetric measurements cannot be applied. Similarly, the correction of "tissue-equivalent" kerma to "tissue" kerma, which arises because of the different compositions of these materials [7], cannot be made because of the same lack of data.

The present report summarizes progress in the calculation of kerma for tissue-resident elements and neutron energies greater than 20 MeV. Section 2 summarizes the methodology and kerma calculations for hydrogen. Section 3 contains descriptions of the theoretical models which have been employed in the calculations. The parameterizations of the models and results for the elements C, N, and O are contained in Section 4, while Section 5 compares the results of the calculations with a dosimetric experiment performed with "NE-213" plastic. This latter section also contains calculated kerma factors for tissue and tissue-equivalent plastic. Conclusions and suggestions for further work are summarized in Section 6.

---

Manuscript submitted July 3, 1980.

## 2. ENERGY TRANSFER TO HYDROGEN

The only charged-particle-producing reaction of significance for neutrons with energies greater than 20 MeV incident upon hydrogen is elastic scattering; it is expected that approximately 50% of the total tissue kerma is due to this process [8].

Conventional Legendre polynomial expansions for the neutron-proton elastic differential cross-section,  $\sigma(\theta)$ , are unavailable in the neutron energy range  $E_n \geq 30$  MeV. There have been, however, extensive energy-dependent determinations of the elastic scattering matrix elements [9,10] which are linear combinations of  $P_l(\theta)$ ,  $P_l^1(\theta)$ , and  $P_l^2(\theta)$ ; in practice,  $l \leq 5$ . The absolute value of the square of the scattering amplitude thus obtained is proportional to  $\sigma(\theta)$ , and either recurrence relations or numerical integration may be employed to obtain the kerma due to elastic scattering

$$K_{el}(E) = \pi N_A A (A + 1)^{-2} E \int_{-1}^1 (1 - \cos \theta) \sigma(\theta) d(\cos \theta), \quad (1)$$

where  $A$  is the mass of the charged recoil relative to that of the neutron, and  $N_A$  is the number of target nuclei per gram. Six-point Gaussian quadrature has been employed for the evaluation of Eq. (1) because the technique is applicable to the elastic and inelastic scattering from the other tissue-resident (TR) elements. Table 1 contains values [11] for the energy transfer to hydrogen in the energy region  $30 \leq E_n \leq 60$  MeV.

Table 1 — Energy Transfer from Neutron to Hydrogen

$E_n$ (MeV)	30	40	60
$K$ [rads/(10 <sup>9</sup> cm <sup>-2</sup> )]	44.53	41.82	37.87

## 3. THEORETICAL MODELS FOR COMPLEX NUCLEI

### A. Optical Model

All of the theoretical models employed for the complex nuclei make use of the optical model in some stage of the calculation. Charged-particle production in the compound nucleus model requires optical model transmission coefficients, while applications of direct reaction models require optical-model distorted wave functions.

In the optical model, the interaction of a free particle and the nucleus is represented by a potential well of the form

$$-U_{opt} = Vf(x) + iWf(x_D) + 4iW_D a_D \left| \left| \frac{d}{dr} f(x_D) \right| \right| + \lambda \frac{2}{\pi} \mathbf{1} \cdot \boldsymbol{\sigma} V_{so} \frac{1}{r} \left| \left| \frac{d}{dr} f(x_{so}) \right| \right| - V_{coul}. \quad (2)$$

In Eq. (2) the signs have been chosen so that the well depths  $V$ ,  $W$ ,  $W_D$ , and  $V_{so}$  are, by convention, positive in the usual case. In general, the well depths are expected to be energy dependent and to contain terms proportional to  $(N-Z)/A$ , where  $N$ ,  $Z$ , and  $A$  are the neutron, proton, and mass numbers of the target nucleus. The shape factors are

$$f(x) = (1 + e^x)^{-1}. \quad (3.1)$$

with

$$x = (r - r_o A^{1/3})/a, \quad (3.2)$$

and similarly for  $x_D$  and  $x_{so}$ . The quantity  $r_o A^{1/3}$  characterizes the radius of the potential,  $a$  its diffusivity, and  $r$  the relative coordinate of the free particle from the nuclear center. The quantity  $V_{coul}$  represents the Coulomb interaction.

The parameters of the model are customarily determined by the fitting of experimental scattering data. The procedures employed in this work are discussed in the succeeding sections devoted to the individual TR elements.

### B. Inelastic Scattering

Some excited states in the TR elements have large cross sections for inelastic scattering compared to those for elastic scattering. In these cases, the contribution of the excited heavy recoil to the total kerma should be included.

In the distorted-wave Born approximation (DWBA), with the assumption that the projectile-target interaction leading to transitions arises from a departure of Eq. (2) from spherical symmetry, the differential cross section for the scattered light particle may be written in terms of the center-of-mass scattering angle as

$$\frac{d\sigma}{d\Omega} = S \frac{\rho}{2l+1} \sum_m \left| \int d^3r \chi_f^-(k_f, r) \frac{\partial U_{opt}}{\partial r} Y_{lm}^*(\hat{r}) \chi_i^+(k_i, r) \right|^2 \quad (4)$$

$$= \sigma(\theta) = S \sigma_{DW}(\theta),$$

where  $l$  is the multipolarity of the transition, the  $\chi_i^+$  and  $\chi_f^-$  are optical-model wave functions for the potential  $U$ , the quantity  $\rho$  is a phase space factor, and  $S$  measures the strength of the transition. In those cases where experimental angular distributions are available, the quantity  $S$  is determined by normalizing theory to experiment.

By means of standard kinematic formulas [12], the angular differential cross section of light particles may be converted to an energy spectrum of heavy recoils.

### C. Analogue Inelastic Scattering Model

The main source of direct reaction protons is emission from low-lying final states of the residual nucleus, which are isobaric analogues of highly excited, particle-unstable, collective states in the target nucleus. When produced, these protons contribute most to the high energy part of the proton spectrum.

It has been assumed that these reactions may be treated with the use of a collective interaction between the free particle and target nucleus, given by [13]

$$\Delta U = \frac{4NZ}{A^2} \left( \frac{\pi}{3} \right)^{1/2} \frac{\partial U_1}{\partial r} \sum_m d_m^+ Y_1^m(\theta, \phi), \quad (5)$$

where  $d$  corresponds to the distance between the centers of mass of the proton and neutron fluids in the Goldhaber-Teller model, and is related to a dipole phonon creation operator  $A_{1m}^+$  by

$$d_m^+ = (\hbar/2\mu m\omega)^{1/2} (A_{1m}^+ + (-)^m A_{1-m}). \quad (6)$$

In Eq. (5), the energy of the dipole oscillation is  $E^* = \hbar\omega$  and  $\mu$  is the reduced mass of the proton and neutron fluids in units of the nucleon mass, while  $U_1$  is the isovector part of the optical potential. The relevant amplitude is then given by

$$S^{1/2} \left\langle \chi_f^- \left| \frac{\partial U_1}{\partial r} \right| \chi_i^+ \right\rangle, \quad (7.1)$$

and the cross section by

$$\sigma(\theta) = S\sigma_{DW}(\theta). \quad (7.2)$$

The optical-model wave functions are  $\chi_i^+$  and  $\chi_f^-$ , angular momentum coupling has been suppressed, and

$$S = 32 \left( \frac{\hbar^2}{2mE^*} \right) \frac{NZ}{A^3}. \quad (8)$$

Equations (6) and (7) have been applied to the analogues of electric dipole transitions in C, N, and O in order to obtain proton emission.

Similar calculations corresponding to the excitation of magnetic dipole transitions have not been attempted because the version of the code DWUCK [14] implemented at NRL has not been modified to include the effect of the tensor force between nucleons. This potential is known to play a central role in comparing both the angular distribution and magnitude of theory and experiment for such transitions. Other versions of the code contain this effect, and such calculations should be performed. For both types of transition, there are two particles in the final states and the contribution of the heavy recoil to the total kerma should be included.

#### D. The $(n,d)$ , $(n,t)$ , $(n,{}^3\text{He})$ Reactions

The total cross sections for the production of  $d$ ,  $t$ , and  ${}^3\text{He}$  tend to be smaller than the production cross sections of protons and alpha particles. Typically,

$$\sigma(n,d) \approx 0.5\sigma(n,p) \quad (9)$$

and

$$\sigma(n,t) \approx \sigma(n,{}^3\text{He}) \approx 0.03\sigma(n,p). \quad (10)$$

The  $(n,t)$  and  $(n,{}^3\text{He})$  reactions will therefore be considered negligible. However, although the deuteron cross section is also rather small, its contribution together with that of the heavy recoil is not negligible.

The  $(n,d)$  reaction receives most of its contribution by the direct pickup of a proton from the target nucleus and may be treated theoretically with a modification of the standard DWBA [15]. This modification includes an approximate treatment of the virtual disintegration of the outgoing deuteron and can reproduce the experimental data satisfactorily. The virtual disintegration of the deuteron is accounted for by replacing  $U_d$ , the deuteron optical potential at energy  $E_d$  in the center of mass system, by the potential

$$\bar{U}_d = (1/D_0) \int d^3s \left\{ U_p(|\mathbf{r} + \mathbf{s}/2|) + U_n(|\mathbf{r} - \mathbf{s}/2|) \right\}_{E=E_d/2} \phi(s) V_{np}(s), \quad (11a)$$

where

$$D_o = \int d^3s \phi(s) V_{np}(s). \quad (12)$$

In Eqs. (11) and (12), the neutron and proton optical potentials  $U_p$  and  $U_n$  are to be evaluated at one-half of the deuteron energy; the deuteron wave function is  $\phi(s)$ , and the neutron-proton interaction is  $V_{np}(s)$ . If  $V_{np}$  is of zero range, Eq. (11a) reduces to

$$\bar{U}_d = [U_p(r) + U_n(r)]_{E=E_d/2}, \quad (11b)$$

where the well depths, energy dependencies, and geometries for the proton term may be obtained from the neutron potentials and reaction Q-values.

The calculations have, in fact, been carried out in a finite-range, nonlocal, volume-concerning approximation, and the DWBA cross section thus obtained,  $\sigma_{dw}$ , has been normalized by a strength  $C^2 S$  which has been obtained from independent nuclear structure calculations [16].

### E. Compound Nucleus Reactions

In the present context, any nuclear reaction which is neither shape elastic scattering given by the optical model nor a single-step direct reaction given by the DWBA is subsumed into the category of compound nucleus reaction. This accounts for most of the protons and alpha particles that are produced; in particular, the  $^{12}\text{C}(n, n'3\alpha)$  reaction belongs to this class of reaction.

The model of compound nucleus reactions which has been adapted [17] is a multistep Hauser-Feshbach model [18] with pre-equilibrium effects treated by the master equation formulation of the exciton model [19].

With the indication of all relevant quantum numbers except energy by  $\alpha, \beta, \dots$ , and of the energy corresponding to state  $\alpha$  by  $\epsilon_\alpha$ , the cross section for a nuclear reaction leading from channel  $\alpha$  to channel  $\beta$  is schematically given by

$$\sigma(\alpha \rightarrow \beta) = [\pi \lambda_\alpha^2 T_\alpha(\epsilon_\alpha)] \left\{ [T_\beta(\epsilon_\beta) \rho_\beta(\epsilon_\beta)] \left[ \sum_\beta T_\beta(\epsilon_\beta) \rho_\beta(\epsilon_\beta) \right]^{-1} \right\}. \quad (13)$$

In this equation,  $\lambda_\alpha$  is the neutron reduced-Compton wavelength, and  $T_\alpha(\epsilon_\alpha)$  is the model "sticking probability"; therefore, the first factor is the probability of forming a compound nucleus. Similarly, the quantity within brackets on the second line is the probability of decay of the compound system with emission of particle  $\beta$  at energy  $\epsilon_\beta$ , and the sum is extended over all states into which the compound system may decay. The level density of the residual nuclear system is allowed to deviate from a standard equilibrium form [20] by a fraction obtained from the master equations that reflect the approach to equilibrium. The level density is taken to be

$$\rho_\beta(\epsilon_\beta) = [1 - f(E)] \rho_{\beta o}(\epsilon_\beta) + \sum_p f(p, h, E) \Omega(p, h, \epsilon_\beta), \quad (14)$$

where

$$f(E) = \sum_p f(p, h, E) \quad (15)$$

is obtained from the master equations, the equilibrium level density is  $\rho_{\beta o}$ , and  $\Omega(p, h, \epsilon_\beta)$  is the density of levels with  $p$ -particles and  $h$ -holes at excitation  $\epsilon_\beta$ .

## 4. RESULTS FOR INDIVIDUAL ELEMENTS

## A. Carbon

Because neutron elastic scattering data have not been obtained in the course of this work, an optical potential was determined by simultaneously fitting neutron and proton elastic and inelastic scattering data which were available in the literature [21-24]. For a fixed geometry, and spin-orbit well depth  $V_{so}$ , the individual best-fit well-depth parameters were then fitted to a linear function of the bombarding energy yielding for  $^{12}\text{C}$  in the energy region  $20 \leq E \leq 60$  MeV

$$\begin{aligned}
 V &= 61.0 - 0.375 E \text{ MeV}, \\
 W &= 4.0 - 0.033 E \text{ MeV}, \\
 W_D &= 1.25 + 0.0167 E \text{ MeV}, \\
 R_o = R_{so} &= 1.069 A^{1/3} \text{ fm}, \quad R_D = 1.354 A^{1/3} \text{ fm}, \\
 a = a_{so} &= 0.647 \text{ fm}, \quad a_D = 0.731 \text{ fm},
 \end{aligned} \tag{16}$$

where all quantities are defined in connection with Eqs. (2) and (3). The angular distribution  $\sigma(\theta)$  predicted by the optical potential may be integrated according to Eq. (1) to obtain the elastic contribution to the kerma. Neutron elastic scattering from  $^{12}\text{C}$  at a bombarding energy of 18.25 MeV is compared with the best-fit optical-model prediction and that of Eq. (16) in Fig. 1; the kerma due to elastic scattering calculated from Eq. (16) is shown in Fig. 2, where it is seen that the dashed extrapolation crosses the experimental point [25]. The effect of inelastic scattering to the 4.44 MeV excited  $2^+$  state has been included in the calculation of Table 2.

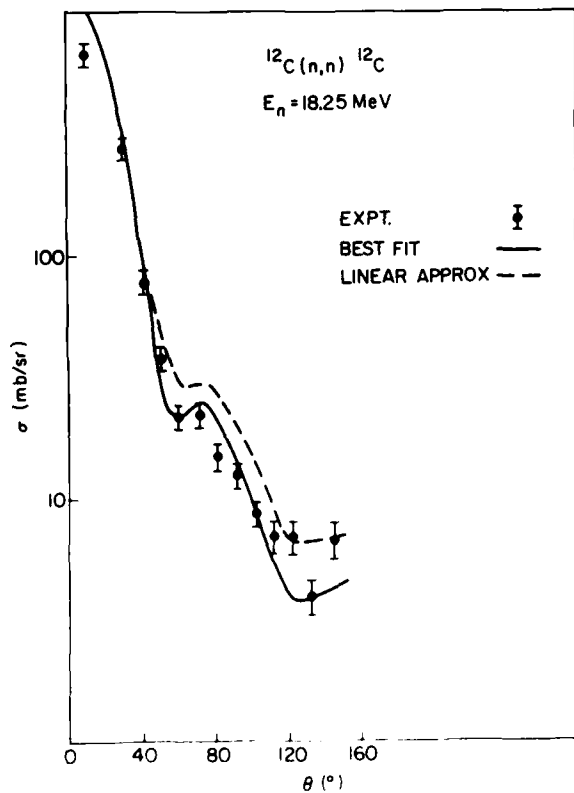


Fig. 1 — Neutron elastic scattering from  $^{12}\text{C}$ . The best fit optical model prediction is indicated by the solid curve, while the dashed curve is the cross section predicted by Eqs. (16). The experimental data are from Ref. 21.

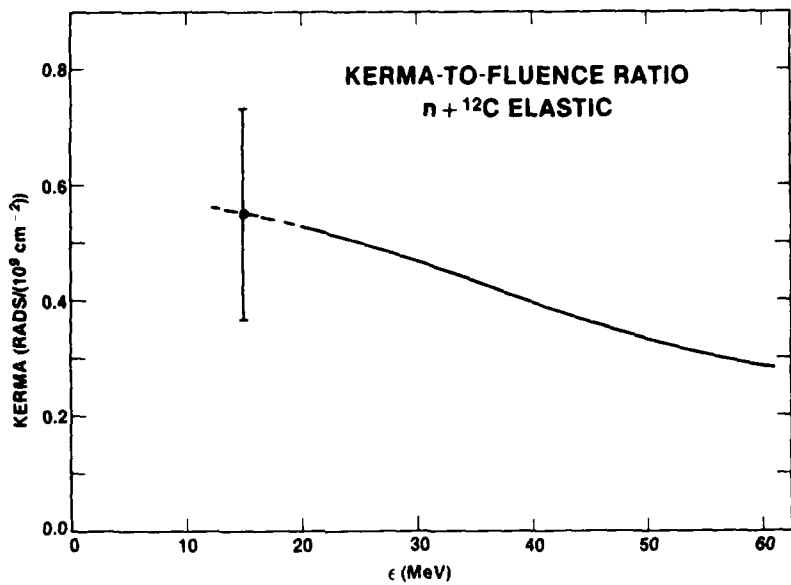


Fig. 2 — Elastic contribution to the carbon kerma calculated with the cross section predicted by Eqs. (16). The experimental point is from the Legendre polynomial fit of Ref. 25, and the dashed part of the curve is extrapolated from the solid part.

Table 2 — Energy Transfer from Neutrons to  $^{12}\text{C}$  Products in Units of Rads/( $10^9 \text{ cm}^{-2}$ )

$E_n (\text{MeV}) \backslash \text{Products}$	27.4	39.7	60.7
p	0.50	0.91	1.51
d	0.59	0.99	0.65
t	-	-	-
$^3\text{He}$	-	-	-
$^4\text{He}$	2.31	2.34	1.71
$^{12}\text{C}$	0.48	0.40	0.28
Total	3.88	4.64	4.15

The contribution of protons to the total kerma has both a direct part and a compound nucleus part. The direct part includes only the analogue of the inelastic scattering to the electric dipole giant resonance (GDR) in  $^{12}\text{C}$  using the optical potential of Eqs. (16), and a final-state modification for the isospin dependence of the optical potential [26]. The calculations have been normalized according to Eq. (8) with  $E^* = 18.2 \text{ MeV}$ , a mean value for the excitation energy of the resonance. Although one could, in principle, treat the excitation of the ground state of  $^{12}\text{B}$  within a similar framework, the direct reaction code employed does not include the effect of the tensor force, which implies an uncertainty in the normalization. Consequently, it has been omitted.

The compound nucleus contributions of protons and alpha particles have been treated according to the discussion of Section 3E, with the inclusion of the  $(n,n)$ ,  $(n,p)$ ,  $(n,\alpha)$ ,  $(n,n')$ ,  $(n,2n)$ ,  $(n,n'p)$ .

$(n, n'\alpha)$ ,  $(n, n'\alpha\gamma)$ ,  $(n, n'\alpha n')$ ,  $(n, n'\alpha p)$ , and  $(n, n'2\alpha)$  reactions; of these, the last, of course, implies an  $(n, n'3\alpha)$  contribution. This chain is expected to be dominant for alpha-particle emission [27].

The optical potentials were either obtained in the present work or chosen from a recent compendium [28]. The general level density of Ref. 20 was parameterized according to the systematic formulae of that work but with the pairing energy chosen to be  $12/A^{1/2}$  in all cases, and shell corrections determined from a liquid droplet mass formula [29].

Figures 3, 4, and 5 compare the theoretical calculations with experimental data obtained at the University of California, Davis (UCD)\* at a neutron energy of 39.7 MeV. Because kinematic shifts constrain the angles at which experimental data can be obtained, data were obtained at only a selected set of angles; therefore it was assumed that the experimental spectrum observed at the largest angle was entirely due to compound nucleus formation and was isotropic in the laboratory coordinate system. This spectrum, given as  $(d^2\sigma/dEd\Omega)_{\theta=\theta_{\max}}$ , was multiplied by the appropriate solid angle, and the result added to the spectrum obtained by angle-integrating the observed data. It should also be noted that the theoretical calculations have not been convoluted with the 1-MeV (fwhm) neutron beam energy spread.

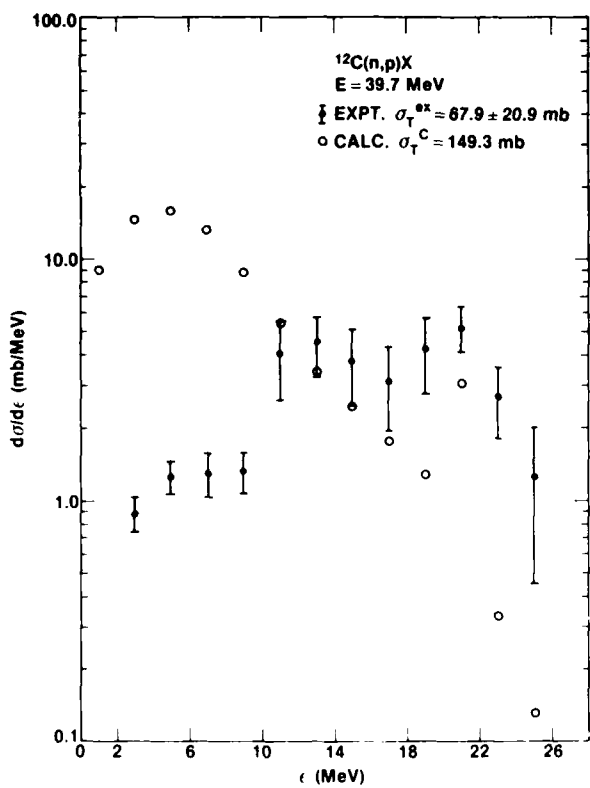


Fig. 3 - Comparison of experimental and theoretical proton spectra from  $^{12}\text{C}$  at a bombarding energy of 39.7 MeV. The experimental data in the form  $(d^2\sigma/dEd\Omega)$  obtained from UCD were treated as described in the text.

\*Note added in proof: The experiment data contained in this report are preliminary. Final data are compared with the theoretical curves in F.P. Brady and J.L. Romero, *Neutron Induced Reactions Tissue Resident Elements*, Crocker Nuclear Laboratory and Department of Physics, University of California, Davis. The agreement between the theoretical curves and experimental data there is generally at least as good as that shown here.

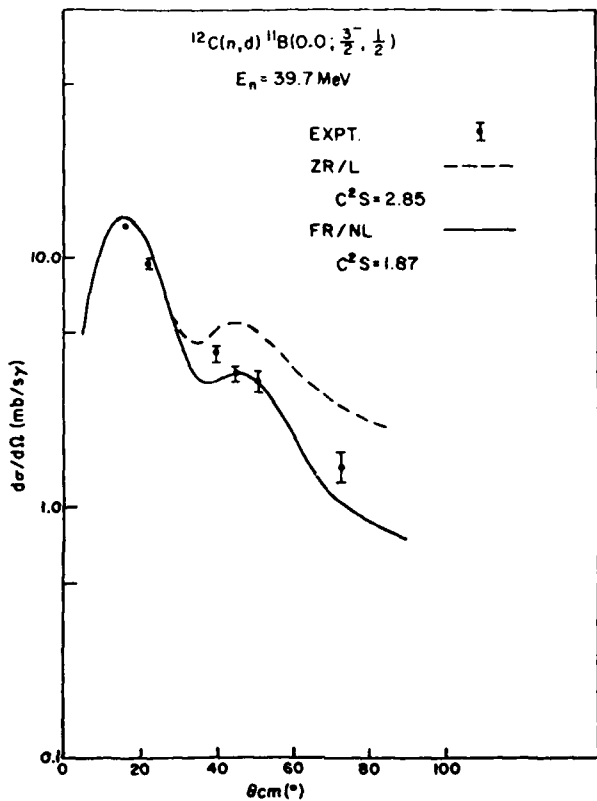


Fig. 4 — Comparison of theoretical and experimental angular distributions for the ground state  $^{12}\text{C}(n,d)^{11}\text{B}$  reaction at a bombarding energy of 39.7 MeV. The dashed curve was obtained with the use of Eq. (11b); the solid curve was obtained with the use of Eq. (11a) supplemented by volume conservation and nonlocality corrections

The excess of calculated low energy protons compared with observation is believed to be an experimental artifact. Necessary gamma-ray discrimination and target energy loss establish lower limits for the energies at which data may be obtained. The plotted points in this energy region are therefore lower limits to the proton production spectrum. The peak in the proton spectrum at 21 MeV corresponds to the excitation of the giant electric dipole resonance in  $^{12}\text{C}$  and illustrates that a direct reaction component must be included if the spectrum is to be fitted. Similarly, the paucity of high energy protons is believed due to the failure to include the analogue of the giant magnetic dipole state in  $^{12}\text{C}$ . Although the basic physical theory for its inclusion is known, it has not been implemented for the present calculations. *It is emphasized that the theoretical calculations are absolute; they have not been normalized to experiment.* Because parameters have been obtained either from systematics or from independent experiments, it would appear that the chosen models are fundamentally adequate for describing the data.

Figure 4 shows a comparison of zero-range/local (ZR/L) and finite-range/non-local (FR/NL) calculations with experimental data obtained at UCD. The spectroscopic strength obtained from the ZR/L calculation is in better agreement with that of Ref. 16 than that obtained from the FR/NL calculation. The better agreement of the FR/NL calculation with the shape of the experimental data, however, suggests that it is the more reliable calculation, and at higher bombarding energies it is known to lead to spectroscopic factors in better agreement with theoretical values.

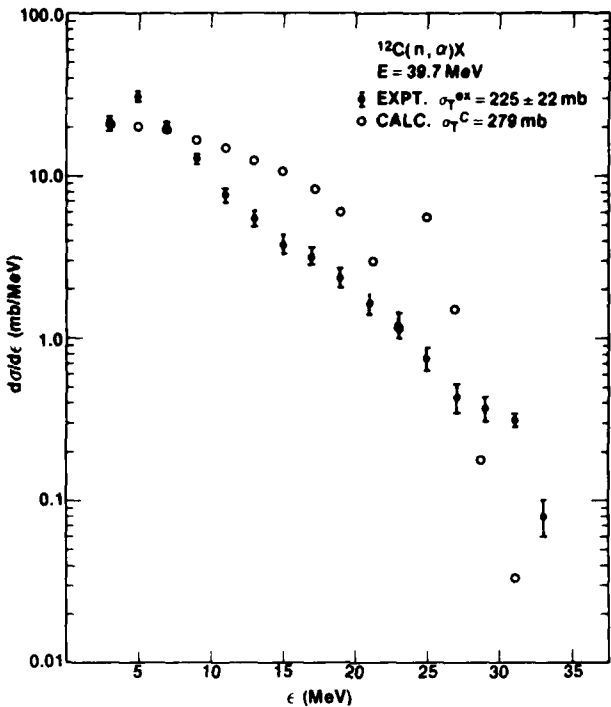


Fig. 5 — Comparison of theoretical and experimental alpha-particle spectra from  $^{12}\text{C}$  at 39.7 MeV. The experimental data from UCD were treated as described in the text.

Figure 5 shows a corresponding comparison of the calculated and experimental alpha-particle spectra. In the present case it is essential that kinematics be treated in detail. Correct kinematics have been included only for the  $(n, \alpha)$  reaction. The parameterization of optical potentials for the calculation of transmission coefficients requires further work, and is probably responsible for the calculated cross section being too large at the intermediate energies. The calculated peak at 25 MeV is presumably due to the assumption that  $^8\text{Be}$  has only a single discrete ground state. The agreement between theory and experiment is considered reasonable for the model chosen.

Table 2 contains the various contributions to the carbon kerma which have been calculated theoretically from the present models. The deuteron contribution to the kerma includes all states calculated in Ref. 16, placed at the experimental binding energies and normalized by the theoretical spectroscopic factors. The energy transfers to both the deuteron and the recoil  $^{10}\text{B}$  nucleus have been taken into account. The results may be compared with other calculations [30,31]. At 27.4 MeV, the present result is in better agreement with that of Ref. 31 than with that of Ref. 30. At 40 MeV, the present result appears to be in good agreement with that of Ref. 30, but at 60 MeV the present result is substantially lower than that of Ref. 30. A complete comparison of the cascade model of Ref. 30, the present model, and experimental cross-section data would therefore be of interest.

### B. Oxygen

Good neutron elastic scattering data were unavailable in the literature, and it was necessary to employ proton data in order to obtain a neutron optical potential. Although it was possible to obtain values of  $\chi^2$  lower than those which have been accepted as yielding "best fits," they are marginally smaller, exhibit some deterioration in the visual fits, and possess somewhat arbitrary geometrical

parameters. This is illustrated in Fig. 6, which contains a comparison of experimental data at 49.48 MeV for the elastic scattering of protons [32] from  $^{16}\text{O}$  with optical model fits. The best fit, which is shown by the dashed curve, was obtained by searching on the three well depths  $V$ ,  $W$ , and  $W_D$ , and on the four geometrical parameters  $R_o$ ,  $a$ ,  $R_D$ , and  $a_D$ , while the solid curve was obtained by searching on the well depths only with the geometry constrained to be [33]

$$\begin{aligned} R_o &= R_{so} = 1.14 A^{1/3} \text{ fm}, & R_D &= 1.40 A^{1/3} \text{ fm}, \\ a &= a_{so} = 0.68 \text{ fm}, & a_D &= 0.45 \text{ fm}. \end{aligned} \quad (17)$$

Although the dashed curve is a slightly better fit to the data than the solid one, it has been obtained at the sacrifice of increasing the number of search variables from four to seven, and the parameters are subject to the uncertainties associated with known ambiguities.

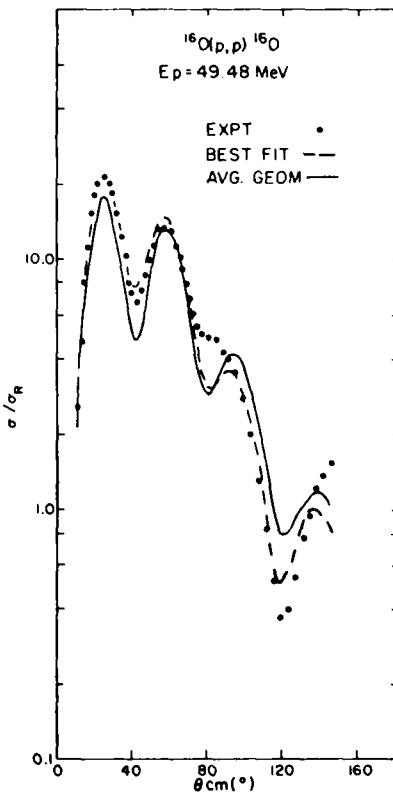


Fig. 6 — Comparison of proton elastic scattering at 49.48 MeV [32] from  $^{16}\text{O}$  with optical model calculations. The dashed curve was obtained from a seven-parameter search, while the solid curve was obtained from a three-parameter search.

With the geometry constrained to the values given by Eqs. (17), and with  $V_{so}$  fixed at 7.0 MeV, searches on  $V$ ,  $W$ , and  $W_D$  were performed for data at 49.48 [32], 46.1 [34], 30.1 [34], and 20.7 MeV [35]. The results of these searches were then fitted by least squares to second-degree polynomials in energy with the results that

$$\begin{aligned} V &= 58.645 - 0.528E + 0.00237E^2, \\ W &= -2.348 + 0.1381E + (3.52 \times 10^{-5})E^2, \\ W_D &= 9.107 - 0.1747E + (7.98 \times 10^{-4})E^2, \end{aligned} \quad (18)$$

where all energies are in MeV. It is emphasized that Eqs. (18) apply to protons and only in the energy range  $20 \leq E \leq 50$  MeV. The low energy behavior of both  $W$  and  $W_D$  is unsatisfactory, and, in fact,

for  $E < 15$  MeV the sign of  $W$  is incorrect. In order to convert these results to a neutron optical potential, Coulomb contributions must be subtracted from the proton optical potential. The final result for neutrons in the energy region  $20 \leq E \leq 50$  MeV is the average potential given by

$$\begin{aligned}
 V &= 57.38 - 0.528E + (2.37 \times 10^{-3})E^2 \text{ MeV}, \\
 W &= -2.348 + 0.1381E + (3.52 \times 10^{-5})E^2 \text{ MeV}, \\
 W_D &= 9.107 - 0.1747E + (7.98 \times 10^{-4})E^2 \text{ MeV}, \\
 V_{so} &= 7.0 \text{ MeV}, \\
 R_o = R_{so} &= 1.14A^{1/3} \text{ fm}, \quad R_D = 1.40A^{1/3} \text{ fm}, \\
 a = a_{so} &= 0.68 \text{ fm}, \quad a_D = 0.45 \text{ fm}.
 \end{aligned} \tag{19}$$

The elastic scattering of protons at 30.1 MeV from  $^{16}\text{O}$  is compared with experiment [34] in Fig. 7. The solid curve was obtained by searching a  $V$ ,  $W$ , and  $W_D$  with the geometry fixed by Eqs. (17). The dashed curve, which is nearly as good a fit as the solid, was obtained from Eqs. (17) and (18), and justifies the choice of Eqs. (19) as the neutron optical potential.

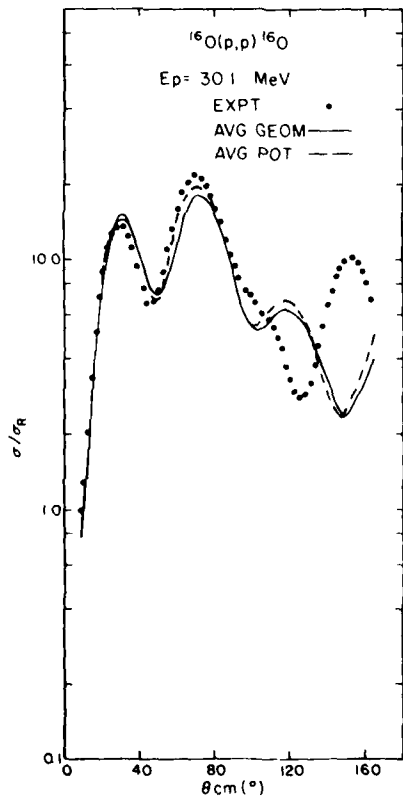


Fig. 7. — Comparison of proton elastic scattering at 30.1 MeV [34] with optical model calculations for  $^{16}\text{O}$ . The solid curve was obtained from a three-parameter search, while the dashed curve was obtained from Eq. (19).

The direct contribution of protons was calculated assuming that this fraction of the  $^{16}\text{O}(\text{n},\text{p})^{16}\text{N}$  reaction proceeds by means of excitation of the analogue of the GDR in  $^{16}\text{O}$ , which occurs at a mean excitation energy of 17.2 MeV. The optical potential of Eqs. (19) was used for the initial state, and the isospin correction of Ref. 26 was applied to obtain the final state optical potential. The direct population of the  $^{16}\text{N}$  ground state would correspond to the analogue of a magnetic quadrupole transition and is presumed weak.

The compound nucleus contributions to proton and alpha-particle spectra were also treated according to Section 3E with the inclusion of the  $(n,n')$ ,  $(n,p)$ ,  $(n,\alpha)$ ,  $(n,n\gamma)$ ,  $(n,2n)$ ,  $(n,np)$ ,  $(n,n\alpha)$ ,  $(n,n\alpha\gamma)$ ,  $(n,n\alpha n)$ ,  $(n,n\alpha p)$ ,  $(n,n2\alpha)$ ,  $(n,n2\alpha\gamma)$ ,  $(n,n2\alpha n)$ ,  $(n,n2\alpha p)$ ,  $(n,n3\alpha)$  reactions; of these, the last implies the  $(n,n'4\alpha)$  reaction.

Figure 8 compares the observed proton spectrum at a bombarding energy of 60.7 MeV with that calculated. The calculated low energy peak in the cross sections is typical of evaporation processes. The calculated peak near 45 MeV corresponds to the centroid of the 4.39 and 4.72 MeV,  $J'' = 1^-$  states of  $^{16}\text{N}$ , but the calculated cross section between 25 and 40 MeV is too small. The experimental data suggest the presence of perhaps three well-defined states, but the density of levels in  $^{16}\text{O}$  is so high that it is difficult to determine which analogue states are receiving a direct reaction contribution without higher energy resolution data with improved statistics.

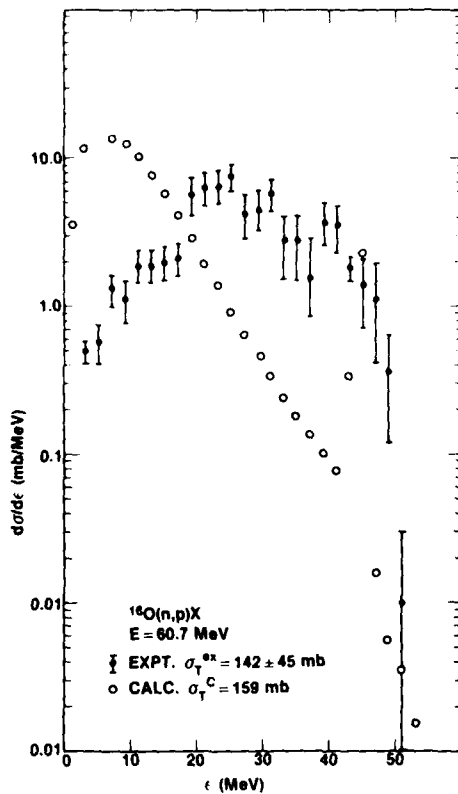


Fig. 8 — Comparison of theoretical and experimental proton spectra from  $^{16}\text{O}$  at a bombarding energy of 60.7 MeV. The experimental data obtained from UCD were treated as described in the text.

Figure 9 contains a comparison of the theoretical and experimental alpha-particle spectra obtained at 60.7 MeV. Although there is a gross failure to reproduce the observed low energy evaporation peak, there is reasonable agreement between theory and experiment for alpha-particle energies greater than 15 MeV. It must be recalled, however, that proper multibody kinematics have not been employed for the calculations. Similarly, not all paths, originating in  $^{17}\text{O}$  and containing open reaction channels, which reach a given final nucleus have been included in the calculations. Both effects may be expected to alter the theoretical results.

Table 3 contains the energy transfer to  $^{16}\text{O}$  in the energy region of interest. In this case the present results at 27.4 MeV are in better agreement with those of Ref. 30 than with those of Ref. 31.

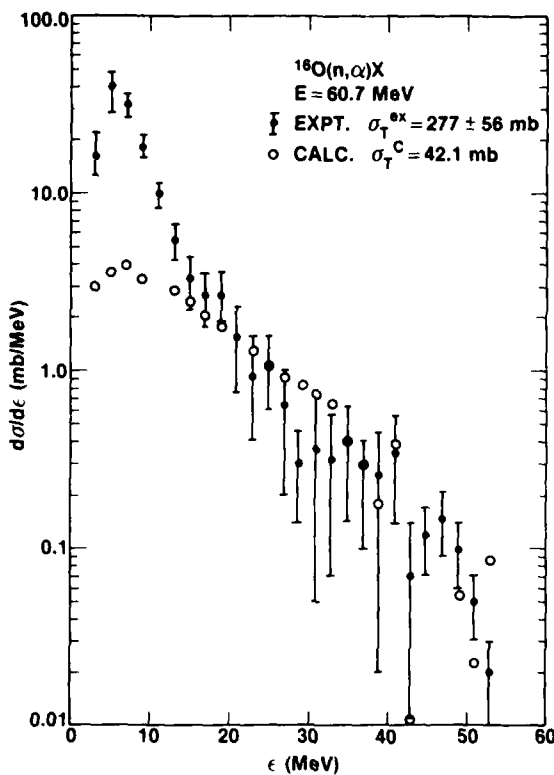


Fig. 9 — Comparison of theoretical and experimental alpha-particle spectra from  $^{16}\text{O}$  at a bombarding energy of 60.7 MeV. The experimental data obtained from UCD were treated as described in the text.

Table 3 — Energy Transfer from Neutrons to  $^{16}\text{O}$  Products in Units of Rads/( $10^9 \text{ cm}^{-2}$ )

$E_n (\text{MeV}) \backslash$ Products	27.4	39.7	60.7
p	0.62	0.78	0.99
d	0.06	0.20	0.26
t	-	-	-
$^3\text{He}$	-	-	-
$^4\text{He}$	0.83	0.72	0.50
$^{16}\text{O}$	0.30	0.24	0.19
Total	1.81	1.94	1.94

At the higher energies, the present results are substantially lower than those of Ref. 30, and just as in the case for  $^{12}\text{C}$ , a detailed comparison of the two calculational methods would be of interest.

### C. Nitrogen

There is a lack of recent elastic scattering data for nucleons in the 20 – 60 MeV energy range from  $^{14}\text{N}$ . However, an analysis of two nucleon transfer reactions with light nuclei [36] has yielded energy-dependent optical potentials for proton scattering from both  $^{13}\text{N}$  and  $^{15}\text{N}$ . The energy dependencies of the potentials are sufficiently different so that attempting to extract a symmetry potential, which would be useful, for example, in calculations of the  $(n,p)$  reaction, would be unreliable. The work of Ref. 36 also considers  $^{14}\text{N}$ , and applying Coulomb corrections to the well depth of the potential  $^{14}\text{N-PI}$  of that work yields the  $n - ^{14}\text{N}$  optical potential for the neutron energy region  $18 \leq E_n \leq 50$  MeV,

$$V = 59.84 - 0.35E \text{ MeV}$$

$$W = -5.1 + 0.17E \text{ MeV}$$

$$W_D = 6.1 - 0.035E \text{ MeV}$$

$$V_{so} = 5.65 \text{ MeV}$$

(20)

$$R_o = 1.11 A^{1/3} \text{ fm}, \quad R_D = 1.36 A^{1/3} \text{ fm}, \quad R_{so} = 1.0 A^{1/3} \text{ fm},$$

$$a = 0.644 \text{ fm}, \quad a_D = 0.52 \text{ fm}, \quad a_{so} = 0.53 \text{ fm},$$

with the restriction that if the neutron energy predicts a negative value for a well depth, it is set equal to zero.

The proton spectrum is treated in the manner previously described in connection with the other TR elements. The direct contribution has been taken to be produced by excitation of the 8.06 MeV  $J^\pi = 1^-$  state of  $^{14}\text{N}$ , which is the analogue of the 6.09 MeV,  $J^\pi = 1^-, T = 1$  state of  $^{14}\text{C}$ . The compound nucleus part of the spectrum includes protons produced in the  $(n,p)$ ,  $(n,p\gamma)$ ,  $(n,pn)$ ,  $(n,2p)$ ,  $(n,p\alpha)$ ,  $(n,pn\gamma)$ ,  $(n,pnp)$ ,  $(n,pn\alpha)$ , and  $(n,p2nx)$  reactions, where  $x$  may be  $\gamma, n, p, \alpha, \alpha\gamma, \alpha n, \alpha p, 2\alpha$ . This particular chain was presumed to be the most probable of several possibilities because of the positive Q-value for the single step  $(n,p)$  reaction, and because the later stages follow the emission of a (virtual) triton that may be thought of as being formed by the incident neutron and a quasi-deuteron outside of a  $^{12}\text{C}$  core.

Figure 10 compares the calculated and observed proton spectra at a bombarding energy of 39.7 MeV. The calculated cross section is higher than that observed for energies less than 10 MeV, but it appears likely that this is due to the low energy experimental cutoff. The peak at 31 MeV is due to the 6.09-MeV excited state of  $^{12}\text{C}$ , and is somewhat larger than that observed. The calculated spectrum is lower than that observed at the highest energies, but for reasons previously mentioned, there has not been an attempt to calculate the analogues of magnetic dipole transitions. In the present case, such a transition would add to the population of the  $J^\pi = 0^+, T = 1$  ground state of  $^{14}\text{C}$ .

Figure 11 compares the theoretical and experimental alpha-particle spectra at the bombarding energy of 39.7 MeV. The alpha-particle optical potential for the  $^{14}\text{N} (n,\alpha)^{11}\text{B}$  reaction was not taken from neighboring nuclei but is one which has had some success with heavier nuclei [37]. Reasonable

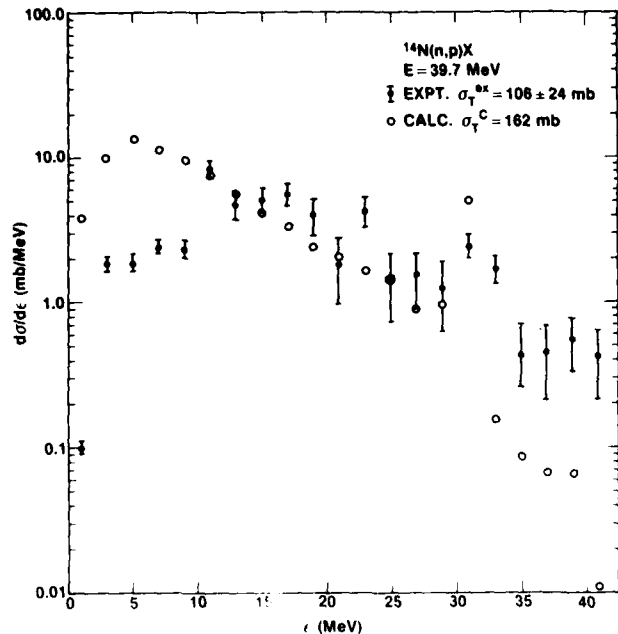


Fig. 10 — Comparison of theoretical and experimental proton spectra from  $^{14}\text{N}$  at a bombarding energy of 39.7 MeV. The experimental data from UCD were treated as described in the text.

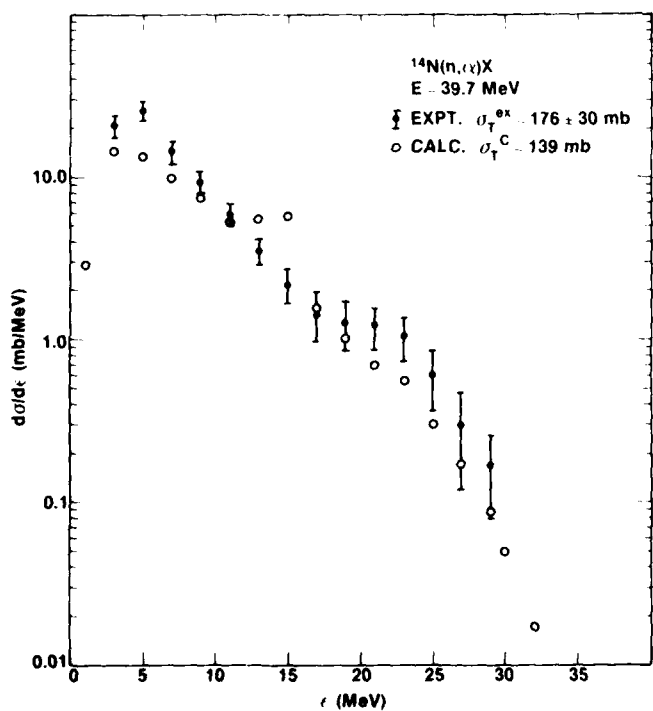


Fig. 11 — Comparison of theoretical and experimental alpha-particle spectra at a bombarding energy of 39.7 MeV. The experimental data from UCD were treated as described in the text.

agreement with experiment is obtained except for the calculated peak at 15 MeV. Similar to the case in  $^{16}\text{O}$ , this is possibly due to the artificial nature of employing continuous level density formulae for systems as light as those considered during evaporation from the TR elements. Similarly, inspection of cross section data indicates the difficulties of applying general models to the analysis of these reactions.

The deuteron contribution to the kerma has been obtained by including all of the appropriate stripping states of Ref. 16, placed at the experimental excitation energies and normalized by the theoretical spectroscopic factors. The calculation includes the kerma of the recoil  $^{13}\text{C}$  nucleus.

Table 4 contains the energy transfer to  $^{14}\text{N}$  in the energy region of interest.

Table 4 — Energy Transfer from Neutrons  
of  $^{14}\text{N}$  Products in Units of Rads/( $10^9 \text{ cm}^{-2}$ )

$E_n (\text{MeV})$	27.4	39.7	60.7
Products			
p	0.93	1.28	1.73
d	0.93	1.05	0.45
t	-	-	-
$^3\text{He}$	-	-	-
$^4\text{He}$	0.53	0.76	1.35
$^{14}\text{N}$	0.38	0.30	0.21
Total	2.77	3.39	3.74

## 5. KERMA FACTORS

In an interesting experiment, time-of-flight techniques and pulse shape discrimination have been employed to measure the contributions of protons and alpha particles to the kerma produced by a neutron beam employed for radiotherapy impinging upon NE-213 plastic [38]. Table 5 compares the experimental results with theoretical results obtained in the present report. The kerma factors for protons and alpha particles are given by

$$K_p = f_H K_H + f_C K_C(P)$$

and

$$K_\alpha = f_C K_C(\alpha),$$

where  $f_H$  and  $f_C$  are the weight fractions of hydrogen and carbon and the factors  $K_H$ ,  $K_C(P)$ , and  $K_C(\alpha)$  are from Tables 1 and 2. The theoretical and experimental proton contributions are in fair agreement with each other, but the theoretical alpha-particle contribution is considerably larger than that observed. The theoretical value is, however, in fair agreement with that of Ref. 31.

Table 5 — Theoretical and Experimental Kerma Factors  
in NE-213 Plastic\*

Kerma Factors	$K_p^{\text{ex}}$	$K_p^{\text{th}}$	$K_\alpha^{\text{ex}}$	$K_\alpha^{\text{th}}$
$E_n (\text{MeV})$				
30	$4.37 \pm 0.66$	4.54	$0.76 \pm 0.11$	2.31
40	$4.00 \pm 0.60$	4.67	$0.66 \pm 0.10$	2.13

\* The experimental data from Ref. 38 are given in rads/( $10^9 \text{ cm}^{-2}$ )

The theoretical quantities of Tables 1-4 may be employed for the calculation of kerma factors for tissue and tissue-equivalent plastic according to

$$K(E) = \sum_L f_L K_L(E), \quad (21)$$

where  $f_L$  is the weight fraction of element  $L$  in the material of interest, and  $K_L(E)$  is given by the last row of the relevant table as a function of neutron energy  $E$ . Models for muscle and tissue-equivalent plastic are given in Table 6, and Table 7 contains the final kerma factors. The kerma factors for tissue are consistently lower than those for plastic primarily because of the enhanced deuteron and alpha-particle production from carbon relative to that from oxygen. The present calculations suggest that for these models, the plastic-to-tissue dose conversion factor is of the order of 0.8 in the 20-60 MeV neutron energy range.

Table 6 — Weight Fractions for Muscle and Tissue-Equivalent Plastic\*

Element	Muscle	Plastic
H	0.10	0.10
C	0.12	0.76
N	0.04	0.04
O	0.73	0.05

\*Ref. 7. Heavier trace elements have been neglected in the present work, and it is assumed that only the most naturally abundant isotope need be considered.

Table 7 — Kerma-to-Fluence Ratios for Tissue and Tissue-Equivalent Plastic\*

$E_n$ (MeV)	Muscle	Plastic
27.4	6.42	7.67
39.7	6.30	7.95
60.7	5.84	7.17

\*Rads/( $10^9$  cm $^{-2}$ )

The data of Table 7 may be conveniently summarized by

$$K_t(E) = R(E) K_p(E), \quad (22.1)$$

where

$$R(E) = 0.84 - (5.0 \times 10^{-4}) E_{MeV} \quad (22.2)$$

is understood to be applied for  $20 \leq E \leq 60$  MeV, and  $K_t$  and  $K_p$  are tissue and plastic kerma, respectively.

## 6. CONCLUSION

Obtaining kerma factors for C, N, and O for neutron energies greater than 20 MeV is difficult. In order to more firmly parameterize possibly applicable nuclear models, data should be obtained with higher neutron energy resolution and improved statistical accuracy in order to resolve individual nuclear states which receive direct reaction contributions. Whenever possible, surrogate proton data, which may be obtained more readily than neutron data, may be employed, and isobaric spin invariance invoked in order to obtain corresponding neutron information.

It is likely that because of intensity limitations, future neutron experiments will necessarily be inclusive, but certain specific reactions such as  $^{12}\text{C}(n,n'3\alpha)$  or  $^{16}\text{O}(n,n'4\alpha)$  should be checked at one energy as exclusive reactions. Such kinematically complete, multiparticle coincidence experiments are difficult and costly, but would serve to establish normalizations and increase confidence in calculations.

## 7. ACKNOWLEDGMENTS

The authors are deeply indebted to F.H. Attix for bringing this problem to their attention. They also wish to thank F.P. Brady, J. Romero, and T.S. Subramanian, their colleagues at UCD, for sending their data to them prior to publication. They are grateful to L.S. August, M. Rosen, and P. Shapiro for helpful discussions. They especially wish to thank C.Y. Fu and P.D. Kunz for allowing them to obtain statistical model and direct reaction codes.

## REFERENCES

1. M. Catterall, *Conf. on Particle Accelerators in Radiation Therapy*, LA-5180-C, 135 (1973).
2. R.B. Theus, *Conf. on Particle Accelerators in Radiation Therapy*, LA-5180-C, 82 (1973).
3. P.R. Almond, *Conf. on Particle Accelerators in Radiation Therapy*, LA-5180-C, 88 (1973).
4. ICRU Report 27, *An International Neutron Dosimetry Intercomparison*, International Commission on Radiation Units and Measurements, Wash., D.C., 1978.
5. J.J. Broerse, G. Burger, and M. Cappola, *Basic Physical Data for Neutron Dosimetry*, Commission of the European Communities, Luxemburg 1976, p. 257.
6. D. Garber, ENDF/B Summary Documentation, BNL 17541 (ENDF-201), 1975.
7. W.A. Glass and W.A. Gross, *Topics in Radiation Dosimetry*, Radiation Dosimetry, Suppl. 1, F.H. Attix, ed., Academic Press, New York, 1972, p. 239.
8. H. Bichsel, J. Eenma, K. Weaver, and P.B. Wooton, in *Particle Radiation Therapy, Proceedings of an International Workshop*, V.P. Smith, ed., American College of Radiology, Philadelphia, 1975, p. 71.
9. R.E. Seamon, K.A. Friedman, G. Breit, R.D. Haracz, J.M. Holt, and A. Prakash, *Phys. Rev.* **165**, 1579 (1968).
10. M.H. MacGregor, R.A. Arndt, and R.M. Wright, *Phys. Rev.* **182**, 1714 (1969).
11. R.H. Bassel and G.H. Herling, *Rad. Res.* **69**, 210 (1977).
12. J.B. Marion and F.C. Young, *Nuclear Reaction Analysis: Graphs and Tables*, Wiley, New York, 1968, p. 140.
13. G.R. Satchler, *Nucl. Phys.* **A195**, 1 (1972).
14. P.D. Kunz (unpublished).
15. R.C. Johnson and P.J.R. Soper, *Phys. Rev.* **C1**, 976 (1970).
16. S. Cohen and D. Kurath, *Nucl. Phys.* **A101**, 1 (1967).

17. C.Y. Fu, in *Symposium on Neutron Cross-Sections from 10-40 MeV*, BNL-NCS-50681, M.R. Bhat and S. Pearlstein, eds. (1977), p. 453.
18. A.E. Sovel'ev, Sov. J. Nucl. Phys. **15**, 154 (1972); Yad. Fiz. **15**, 272 (1972).
19. C. Kalbach, Rapport Interne, DPH-N/BE/74/3, Department de Physique Nucleaire/Basse Energies, C.E.N. Saclay; 91190 Gif-sur-Yvette (1974).
20. A. Gilbert and A.G.W. Cameron, Can. J. Phys. **43** 1446 (1965).
21. G. Deconninck and J.P. Meulders, Phys. Rev. **C1**, 1326 (1970).
22. J.K. Dickens, D.A. Haner, and C.N. Waddell, Phys. Rev. **129**, 743 (1963).
23. L.N. Blumberg, E.E. Gross, A. van der Woude, A. Zucker, and R.H. Bassel, Phys. Rev. **147**, 812 (1966).
24. F.E. Bertrand and R.W. Peele, ORNL-4799 (1973) (unpublished).
25. D.W. Glasgow, F.O. Purser, H. Hogue, J.C. Clement, K. Stelzer, G. Mack, J.R. Boyce, D.H. Epperson, S.G. Buccino, P.W. Lisowski, S.G. Glendinning, E.G. Bilpuch, and H.W. Newson, Nucl. Sci. Eng. **61**, 521 (1976).
26. D.M. Patterson, R.R. Doering, and A. Galonsky, Nucl. Phys. **A263**, 261 (1976).
27. B. Antolkovic and Z. Dolenc, Nucl. Phys. **A237**, 235 (1975).
28. C.M. Perey and F.G. Perey, Atomic Data and Nuclear Data Tables **17**, 1 (1976).
29. W.D. Myers and W.J. Swiatecki, Nucl. Phys. **81**, 1 (1966).
30. R.G. Alsmiller, Jr. and J. Barish, Health Phys. **33**, 98 (1977).
31. ICRU Report 26, *Neutron Dosimetry for Biology and Medicine*, International Commission on Radiation Units and Measurements, Wash., D.C., 1977, App. A.
32. J.A. Fannon, E.J. Burge, D.A. Smith, and N.K. Ganguly, Nucl. Phys. **A97**, 268 (1967).
33. A. Gabric and K. Amos, Austr. J. Phys. **30**, 287 (1977).
34. J.M. Cameron, J.R. Richardson, W.T.H. Oers, and J.W. Verba, Phys. Rev. **167**, 908 (1968).
35. N. Baron, R.F. Leonard, and D.A. Lind, NASA TN-D4932 (1968).
36. M. Pignanelli, S. Micheletti, I. Iori, P. Guazzoni, F.G. Resmini, and J.L. Escudie, Phys. Rev. **C10**, 445 (1974).
37. L. McFadden and G.R. Satchler, Nucl. Phys. **84**, 177 (1966).
38. L.S. August, P. Shapiro, and R.B. Theus, *Cross Sections and Yields for High Energy Neutron Source Reactions*, NBSIR 77-1279, 1977, p. 31.

